Towards Robotic-Assisted Subretinal Injection: A Hybrid Parallel–Serial Robot System Design and Preliminary Evaluation

Mingchuan Zhou, Qiming Yu, Kai Huang, Simeon Mahov, Abouzar Eslami, Mathias Maier, Chris P. Lohmann, Nassir Navab, Daniel Zapp, Alois Knoll, and M. Ali Nasseri

***Abstract*—Subretinal injection is a delicate and complex microsurgery. The main surgical difficulties come from the surgeon's hand tremor, dexterous motion, and insufficient visual feedback. In order to begin addressing these challenges, this article presents a robot system for subretinal insertion integrated with intraoperative optical coherence tomography (OCT). The surgical workflow using this system consists of two main parts. The first part is the manual robot control, which aims the target before approaching the retinal surface, while considering the remote center of motion (RCM) constraint. When the injection area has been located precisely, needle is inserted into retina. To ensure surgical safety, needle insertion depth is estimated using OCT images on a continuous basis. A soft RCM control method is designed and integrated for the controller of our hybrid parallel–serial surgical robot. Safety and accuracy performance evaluation with a 15-ms control loop shows that the worst-case RCM deviation error is within 1 mm. Experimental results demonstrated that the proposed system has the ability to improve surgical outcomes by surgeons overcoming their physical limitations in order to enable a better dexterous motion, and furthermore enhancing their visual feedback for a better intraocular perception.**

***Index Terms*—Biomedical optical imaging, medical control systems, motion control, surgical robot.**

I. Introduction

SUBRETINAL injection has been successfully used in clinical trials to deliver therapeutic cargos of proteins, viral agents, and cells to the interphotoreceptor or subretinal compartment that has direct exposure to photoreceptors and the retinal pigment epithelium (RPE) [1], [2]. This intervention has the potential to create effective outcomes for well-known retinal diseases including age-related macular degeneration (AMD), which is the leading cause of blindness in developed countries [3]. The predicted population with AMD in 2020 is 196 million and will increase to 288 million by 2040 according to [4], due to demographic changes and aging. Subretinal injection is a form of vitreoretinal surgery. In this operation, conventionally, the surgeon is required to inject a microcannula into a specific area of the translucent retina to a certain depth. This area is a target that is normally defined preoperatively by the ophthalmologist (see Fig. 1).

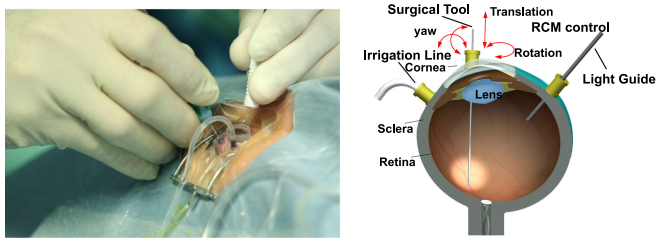

Fig. 1. Conventional subretinal injection setup. The incision ports are made by trocars at the sclera in a circle, which is 3.5 mm away from the limbus, to provide an entrance for surgical tools: Light source, surgical tool, and irrigation line [6]. The light source is used to illuminate the intended area on the retina, allowing its planar view to be analyzed by the surgeon through the ophthalmic microscope. The irrigation line is used for liquid injection to maintain appropriate intraocular pressure.

Subretinal injection is known as a delicate and complex procedure for a surgeon to perform. The surgeon needs several years of training on phantom and clinical trials in order to handle the hand tremor and gain proper dexterous motion, e.g., precision intraocular manipulation, while taking into account remote center of motion (RCM) control to reduce the trauma on the sclera. In addition, the surgeon has to control the depth of the needle tip precisely. Because a shallow injection will not effectively release drug to the subretinal area [5] and an overly deep injection may result in irreparable damage to the RPE and causing vessel rupture. Due to the fact that the retina is a transparent tissue with limited illumination from conventional intraocular

Manuscript received January 15, 2019; revised May 25, 2019 and July 10, 2019; accepted August 7, 2019. Date of publication August 28, 2019; date of current version March 31, 2020. *(Corresponding author: Kai Huang.)*

M. Zhou, Q. Yu, S. Mahov, N. Navab, and A. Knoll are with the Computer Science Department, Technical University of Munich, 85748 Munich, Germany (e-mail: zhoum@in.tum.de; qiming.yu@tum.de; mahov.simeon@tum.de; navab@tum.de; knoll@tum.de).

K. Huang is with the School of Data and Computer Science, Sun Yat-Sen University, Guangzhou 510006, China (e-mail: huangk36@mail.sysu.edu.cn).

A. Eslami is with the Carl Zeiss Meditec AG., 81379 Munich, Germany (e-mail: abouzar.eslami@zeiss.com).

M. Maier, C. P. Lohmann, D. Zapp, and M. A. Nasseri are with the Augenklinik und Poliklinik, Klinikum rechts der Isar, Technical University of Munich, 81675 Munich, Germany (e-mail: athias.maier@mri.tum.de; chris.lohmann@mri.tum.de; daniel.zapp@mri.tum.de; ali.nasseri@mri.tum.de).

Color versions of one or more of the figures in this article are available online at http://ieeexplore.ieee.org.

Digital Object Identifier 10.1109/TIE.2019.2937041

light sources, it is difficult for the surgeon to judge the insertion depth from the traditional microscopic view alone, when the needle tip is under the retinal surface.

To overcome the surgeon's hand tremor and to achieve dexterous motion and precise RCM control, in recent years many researchers have introduced robotic setups with high precision in different scales and design mechanisms [6]–[13]. These robots can be classified into four main categories: 1) Hand-held surgical instruments, which have the benefits of tremor suppression and intuitive operation [14], [15]. 2) Cooperatively controlled systems [9], which focus on tremor filtering with a stable robotic arm, normally equipped with force sensors. Cooperatively controlled systems can be operated intuitively, due to the fact that the surgical tool is held by the robot and the surgeon's hand simultaneously. The use of force sensors in the system allows to have a motion "scaling" in the admittance control scheme. However, they introduce inertial and frictional forces that may limit their application in dynamic tasks. 3) Teleoperation systems, which are often embodied within a console-based setting to provide tremor filtering and motion scaling. These systems are known to be the most successful in the commercial products, e.g., the da Vinci surgical robot (Intuitive Surgical Inc.). However, quite apart from their significant footprints, robots designed for general surgery do not have sufficient precision for retinal surgery [16]. 4) Magnetically controlled microrobots could provide an alternative surgical approach, but their current systems are in a very early stage and lack most of the benefits of robot assistance [17], e.g., safety consideration and haptic feedback [18], [19]. In recent years, ophthalmic robots have matured sufficiently to enter clinical trials. The robotic retinal dissection device with teleoperation functionality performed the world's first robotic subretinal injection in 2016 [17] proving the feasibility and safety concept of the robot-assisted eye surgery. It is still difficult for surgeon to estimate the needle tip position under retina, even though the robot is introduced. The reason is that the system kinematics are not suitable for estimating the needle-tip position accurately, due to a thin, long, and flexible needle body [20] with heterogeneous deformations. Therefore, additional imaging modality is necessary.

In order to tackle the aforementioned challenges, in this article, we designed a hybrid parallel–serial robot integrated with intraoperative optical coherence tomography (OCT) imaging to assist ophthalmologists in performing the subretinal injection with enhanced precision and proper visualization. The robot proposed originally [21] has two parallel units and one prismatic joint. Unlike the mechanical hardware-based RCM mechanisms [22]–[25]; to realize precise and robust software-based RCM control. The benefit of our proposed method is that this kind of mechanism gives rise to a very compact robot (the current functional prototype which weighs 315 grams and its volume is equivalent to the size of an average human hand). This would be easier to integrate in a conventional ophthalmic operation room that is already occupied by several machines. However, the main challenge from this configuration is that the RCM control has to be designed in the "soft" way which means that the robot controller should be able to synchronize all the joint positions in a proper and timely manner with proper constraints. Serious consideration must be given to a safe and critical application scenario in which the RCM point should be controlled within the clinical-grade tolerance so that the trauma to the sclera is minimized. The main contributions of this article are summarized as follows.

1) A light-weight and safety-concerned software RCM control method are designed and verified on the proposed hybrid parallel–serial robot. The overall control loop of the system is within 15 ms. Our results show a tradeoff between the robot moving speed and RCM control accuracy by the proposed method. The worst case of RCM deviation is limited to 1 mm, which is within clinical tolerance referred to 3 mm free-hand error performance [26].
2) A commercial intraoperative OCT is integrated into the robotic system and used to track the needle insertion depth by unitizing the needle localization algorithm from Zhou *et al.* [27]. Preliminary evaluation is performed on the *ex-vivo* pig eye and phantom tissue to verify the feasibility of the workflow.

The rest of this article is organized as follows. Section II introduces the related work. Section III details the mechanical design of the robot, control as well as OCT integration. Section IV presents the verification of the overall system, including the RCM performance and needle insertion tracking with the robot. Section V concludes this article.

II. Related Work

We consider two respects of related work regarding the main contributions of this article. One is the RCM control method and the other is the OCT integration into the robotic system.

The RCM control concept has been investigated by many researchers in multirobot-assisted surgical applications. In particular, the seminal work from Taylor *et al.* [22] proposed the classical design of orthogonally decoupled mechanical structure and also the concept of software-based method to realize the RCM control. The RCM control realization is depended on the selection of the mechanical design. The hardware RCM is ensured by the mechanical structure, while the software RCM depends on the control system design. He *et al.* [28] measured that the steady hand robot has a maximum error of 0.52 mm hardware RCM control accuracy by introducing a specifically designed mechanical roll–tilt mechanism. Kim *et al.* [23] proposed a modified hardware RCM by setting the gear ratio in the ball screw driving mechanism. Compared with the hardware RCM, software RCM has the benefit of more freedom in mechanical design, or even using the available platform. Wei [24] proposed a software RCM control method based on the Stewart–Gough platform which has the benefit of rigid and compact design. Nakano *et al.* [6] proposed a parallel robot design on Stewart–Gough platform to enhance the workspace. They applied the software RCM method to achieve a maximum control error of 1.4 mm. However, these mentioned software RCM can not be directly implemented on our proposed hybrid parallel–serial robot, because of the different design structure. Furthermore, the mentioned work does not consider the safety consideration of the software RCM implantation, e.g., how to

ensure the worst-case deviation of RCM control, which should be serious, considering the medical application.

Three-dimensional ultrasound and MRI imaging, which are typically used in nonmicrosurgical scenarios, are not precise enough for subretinal interventions. These imaging modalities normally offer a needle localization error of around 500 μm [29], while the retina, with an average thickness of around 250 μm [30], requires operational accuracy with a maximum error of 25 μm [31]. OCT was originally used for ophthalmic diagnosis, and has since been modified for intraoperative procedures by offering a suitable resolution with noninvasive radiation entailing the minimum risk of toxication for the ocular tissue. Currently, there are two methods to intraoperatively deploy OCT data for intraocular needle localization. The first method proposed by Cheon *et al.* [32] is to detect the distance of the target surface from the OCT probe using A-scans. Afterwards, the insertion depth can be calculated considering the distance of the needle tip and OCT probe is known. The limitation of this method is that the needle tip needs to be perpendicular to the target surface. Furthermore, the integration of OCT probe into the needle makes the instrument more complicated in process and maintenance. Instead of integrating OCT probe in surgical instrument, the microscope-integrated intraoperative OCT, which share the same path with microscope to capture volumetric images, is used to estimate the needle tip position. The benefit of this method is to avoid using modified needles but utilizing conventional subretinal cannulas. Based on microscope-integrated intraoperative OCT, Zhou *et al.* [27] proposed an algorithm to estimated the needle insertion depth with an maximum error of 16.5 μm. In this article, we integrate this method in our proposed robot system to preliminary verify the overall operation workflow.

III. Method and Materials

A. Robot Design

In order to design a compact and lightweight robot for intuitive integration in the ophthalmic clinical routine, we propose a platform based on the hybrid parallel–serial mechanism designed by prismatic and rotation joints, and realized by using linear stick–slip piezo actuators. The design is originally based on the first prototype [21]. The driving force for choosing this mechanism is the reduction in backdriving effect caused by the gear or the tendon. This effect will be significantly reduced in our mechanism while the joint is directly driven by the motor. The detailed parallel mechanical unit is shown in Fig. 2. The piezo motors M_1 and M_2 with the prismatic joints J_1 and J_2 are mounted in parallel back-to-back which is used to reduced the friction from gravity compared to the previous design [21]. The rotation joints J_3, J_5, and prismatic joint J_4 are used to close the kinematics loop of the unit. The synergetic control of two prismatic joints can be transferred into a virtual prismatic q_0 and rotation joint q_1, which can be calculated as

$$q_0 = L_1 \tag{1}$$

$$q_1 = a\tan\left(\frac{L_2 - L_1}{d}\right) \tag{2}$$

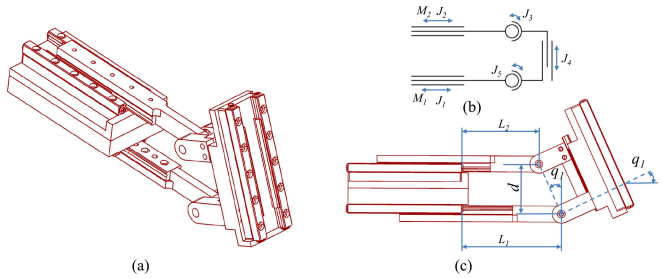

Fig. 2. Parallel mechanical unit. (a) Oblique view of the unit. (b) Structure diagram of the unit. (c) Rotation effect with the front view of the unit with main dimensions.

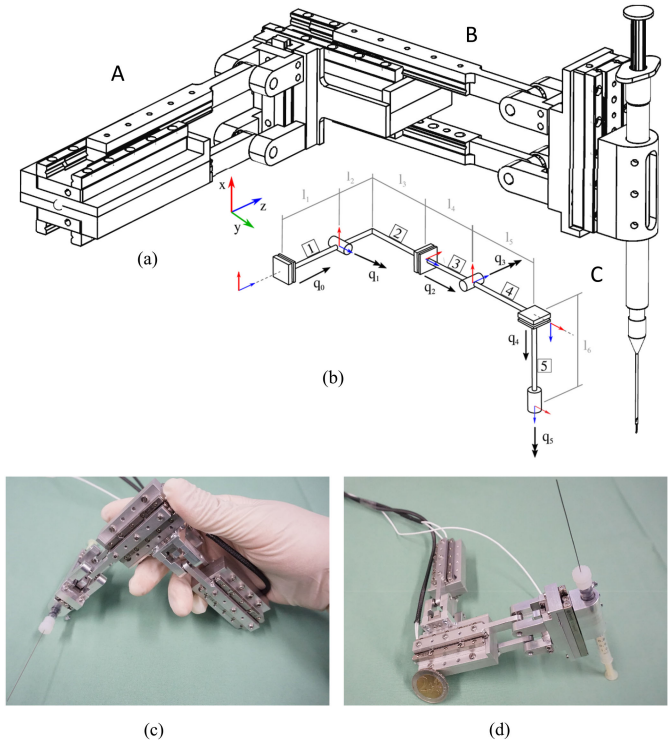

Fig. 3. (a) CAD model of the robot with two identical parallel mechanical units **A**, **B**. **C** is the final prismatic joint, used for decoupled injection. l_1, l_2, l_3, l_4, l_5, and l_6 are the Denavit–Hartenberg parameters. (b) Simplified kinematics structure of the robot. (c) and (d) Real entity of designed robot in different view.

where L_1 is the position of joint J_1 from the initial position, and L_2 is the position of joint J_2 from the initial position. The positive direction of rotation joint q_1 is clockwise.

The robot consists of two parallel mechanical units and a needle slider, comprising a five degree-of-freedom (DoF) manipulator, shown in Fig. 3. Its Denavit–Hartenberg parameters are obtained via the CAD model. A key feature is that its workspace is free of singularities as the mapping between joint vectors and needle poses is one-to-one. Due to this advantage and the plain forward kinematics, spatial coordinates can be stored as joint vectors $\boldsymbol{q}$ for the purpose of a virtual fixture constraint, where $\boldsymbol{q}$ is presented as

$$\boldsymbol{q} = [q_1, q_2, q_3, q_4, q_5]. \tag{3}$$

B. Robot Control and RCM Constraint

The robot is designed to have three types of movement by a master control device. (a) Unconstrained movement: The robot is controlled by a master device without any motion constraint. The movement type (a) is activated when the needle is placed outside of the eye and the robot is controlled to align the needle with the trocar to be introduced inside the eye. (b) RCM control when the needle is inside the eye: as soon as the needle tip approaches the trocar entrance with the correct orientation, normally perpendicular to the scleral surface, the needle-tip position is registered as the RCM point and movement type (b) is activated. The RCM movement type is to reduce the incision point trauma. (c) Insertion mode for needle injection: movement type (c) is enabled when the needle approaches very close to the retina typically around 0.5 mm from needle tip to retina distance. During the injection, only the last degree of freedom, slider q_5, is enabled. The three type of movements can be switched manually by the switch button on the control panel by the surgeon.

The robot movement types (a) and (c) can be directly executed using the PID controller of the master interface. Here we mainly introduce the RCM control algorithm design for our specifically designed robot. To achieve RCM motion, the joint parameters sent to the robot must be such that the end-effector (i.e., the needle) moves through a point in space with minimum deviation. If the operative part of the needle is represented by a unit vector $\widehat{\boldsymbol{n}}$ connecting the needle tip $\boldsymbol{x}_{\text{tip}}$ to a needle "base" $\boldsymbol{x}_{\text{base}}$ (a point remaining outside the eye), the constraint is expressed as

$$\Delta \boldsymbol{x}_{\text{tip}} \cdot \widehat{\boldsymbol{n}} = \Delta \boldsymbol{x}_{\text{base}} \cdot \widehat{\boldsymbol{n}} \tag{4}$$

$$\Delta x_{\text{base}} \times (\boldsymbol{x}_{rcm} - \boldsymbol{x}_{\text{tip}}) = \Delta x_{\text{tip}} \times (\boldsymbol{x}_{rcm} - \boldsymbol{x}_{\text{base}}) \tag{5}$$

where Δx_{base} and Δx_{tip} are the movement for base and tip point in a small time interval, Δx_{tip} is obtained from master control signal, $\boldsymbol{x} = \left[\begin{smallmatrix} \boldsymbol{x}_{\text{tip}} \\ \boldsymbol{x}_{\text{base}} \end{smallmatrix}\right]$ is the current position of the base and needle tip point, which can be calculated from the forward kinematics of the robot, $\boldsymbol{x}_{rcm}$ is the registered RCM point in space, as shown in Fig. 4. The equations state that the tip and the base velocity components along the needle must be equal (conservation of needle length), whereas those perpendicular to the needle are coplanar, in opposite directions, and with magnitudes proportional to the distance from the RCM point to the base point, and the RCM point to the tip point, respectively. These requirements can be integrated when the inverse kinematics are solved in order to control the robot with a two-point kinematic scheme. The needle state is taken as a vector comprising the tip and the base positions, and the translational part of the respective Jacobians is used to iteratively solve

$$\boldsymbol{J} \cdot \Delta \boldsymbol{q} = \begin{bmatrix} \Delta \boldsymbol{x}_{\text{tip}} \\ \Delta \boldsymbol{x}_{\text{base}} \end{bmatrix} = \boldsymbol{x}^{\text{targ}} - \boldsymbol{x} \tag{6}$$

to update the joints difference $\Delta \boldsymbol{q}$, where $\boldsymbol{J} = \left[\begin{smallmatrix} \boldsymbol{J}_{\text{tip}}(\boldsymbol{q}) \\ \boldsymbol{J}_{\text{base}}(\boldsymbol{q}) \end{smallmatrix}\right]$, $\boldsymbol{J}_{\text{tip}}(\boldsymbol{q})$ and $\boldsymbol{J}_{\text{base}}(\boldsymbol{q})$ are the Jacobians for $\boldsymbol{x}_{\text{tip}}$ and $\boldsymbol{x}_{\text{base}}$ respectively. $\boldsymbol{x}_{\text{base}}$ can be calculated based on $\boldsymbol{x}_{\text{tip}}$ and $\boldsymbol{x}_{rcm}$ with the assumption of a straight needle, as follows:

$$\lambda(\boldsymbol{x}_{\text{base}} - \boldsymbol{x}_{\text{tip}}) = \boldsymbol{x}_{\text{base}} - \boldsymbol{x}_{rcm} \tag{7}$$

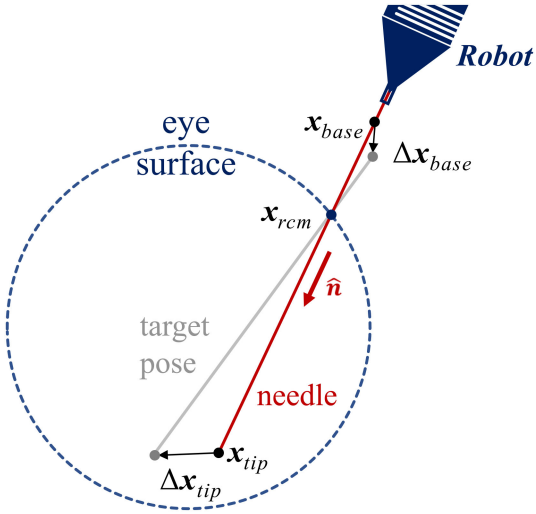

Fig. 4. Schematic showing the change in a straight needle pose as a result of the tip displacement in RCM mode.

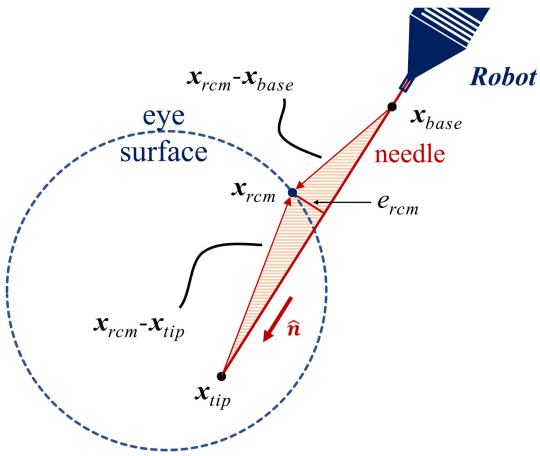

Fig. 5. Forward kinematics and needle detection are used to obtain an estimation for the RCM control error (exaggerated for visual purposes here), proportional to the ratio between the highlighted area and the length of the needle's operative segment.

where λ is the ratio factor that starts from one when the needle tip enters into the trocar. Afterwards, λ will change based on the movement of the needle tip and will be updated with a difference $\Delta\lambda$

$$\Delta\lambda = \Delta \boldsymbol{x}_{\text{tip}} \cdot \widehat{\boldsymbol{n}}. \tag{8}$$

A target state based on desired tip displacement can be constructed

$$\boldsymbol{x}^{\text{targ}} = \begin{bmatrix} \boldsymbol{x}_{\text{tip}} + \Delta \boldsymbol{x}_{\text{tip}} \\ M(\boldsymbol{x}_{\text{tip}} + \Delta \boldsymbol{x}_{\text{tip}}, \boldsymbol{x}_{rcm}, \lambda) \end{bmatrix} \tag{9}$$

where $M(\boldsymbol{x}_{\text{tip}}, \boldsymbol{x}_{rcm}, \lambda)$ is a function refining from (6) for calculating $\boldsymbol{x}_{\text{base}}$. An RCM deviation error, shown in Fig. 5, can

Algorithm 1: RCM Control Algorithm.

INPUT1: $\Delta \boldsymbol{x}_{\text{tip}}$ - Displacement of needle tip
INPUT2: $\boldsymbol{x}_{rcm}$ - Fixed position of RCM point
OUTPUT: $\Delta \boldsymbol{q}$ - Movement for each joint
$getJoints()$ ← Get all the joints' positions
$fwdKinematics()$ ← Update $\boldsymbol{x}$ using forward kinematics
$calcTarget()$ ← Update $\boldsymbol{x}^{\boldsymbol{targ}}$ using (9)
$calcJacobian()$ ← Update Jacobian for (6)
$errorRCM()$ ← Update RCM deviation error with (10)

function rcmstep(Δx_{tip}, x_{rcm})
  $\boldsymbol{q} \leftarrow getJoints()$, $\Delta \boldsymbol{q} \leftarrow \boldsymbol{0}$
  $\boldsymbol{x} \leftarrow fwdKinematics(\boldsymbol{q})$
  $\boldsymbol{x}^{targ} \leftarrow calcTarget(\boldsymbol{x}, \Delta \boldsymbol{x}_{\text{tip}}, \boldsymbol{x}_{rcm})$
  while true **do**
    $\boldsymbol{J} \leftarrow calcJacobian(\boldsymbol{q})$
    $\Delta \boldsymbol{q} \leftarrow \Delta \boldsymbol{q} + \boldsymbol{J}^{\dagger} \cdot (\boldsymbol{x}^{\text{targ}} - \boldsymbol{x})$
    $\boldsymbol{x} \leftarrow fwdKinematics(\boldsymbol{q} + \Delta \boldsymbol{q})$
    $e_{rcm} \leftarrow errorRCM\ (\boldsymbol{x}_{\boldsymbol{rcm}}, \boldsymbol{x}_{\text{tip}}, \boldsymbol{x}_{\text{base}})$
    if $||\boldsymbol{x}^{\text{targ}} - \boldsymbol{x}|| <= \varepsilon_1$ **then**
      if $e_{rcm} > \varepsilon_2$ **then**
        $\Delta \boldsymbol{q} \leftarrow$RCMSTEP($\Delta \boldsymbol{x}_{\text{tip}}/2, \boldsymbol{x}_{rcm}$)
      else
        break
      end if
    else
      $\Delta \boldsymbol{q} \leftarrow \boldsymbol{0}$, break
    end if
  end while
  return $\Delta \boldsymbol{q}$
end function

also be derived using the cross-product-area identity as

$$e_{rcm} = \frac{1}{|\ \boldsymbol{x}_{\text{tip}} - \boldsymbol{x}_{\text{base}}\ |} |\ (\boldsymbol{x}_{rcm} - \boldsymbol{x}_{\text{tip}}) \times (\boldsymbol{x}_{\text{tip}} - \boldsymbol{x}_{\text{base}})\ | \tag{10}$$

which is to be used for step-size control.

Forward kinematics are employed to evaluate (13) between steps to ensure that the RCM control error is within an algorithm control tolerance ε_1 and ε_2 for needle tip and RCM point positions. Combining the aforementioned equations, Algorithm 1, shown below recursively updates joint target positions with given tip displacements. The tolerance ε_1 and ε_2 are dependent on actuator precision and are a tradeoff between the displacement of the needle tip in small time intervals, and the quality of virtual-fixture adherence. The algorithm will first check whether the target position can be reached by the movement of joints. Then, a check is performed on the mid-step RCM deviation, resulting in a recursive decrease in step size or execution of the update if e_{rcm} is within tolerance.

C. Master and Slave Control Design

The control signal from the master controller can be treated as $\boldsymbol{m} = [m_1, m_2, m_3, m_4, m_5]$, where m_1, m_2, and m_3 are the translation speed input, and m_4 and m_5 are the rotation speed input. We use the joystick as the master controller. Due to the fact that some random unintentional movements are made in other directions while motion is controlled by the joystick, the input signal is taken from the maximum value in $\boldsymbol{m}$. The speed and acceleration for the translation and rotation of the needle need to be constrained within the range of motor dynamic character, shown as follows:

$$s = \begin{cases} \max(\boldsymbol{m}), \text{if } \max(\boldsymbol{m}) < \boldsymbol{V}_{\max} \\ \boldsymbol{V}_{\max}, \text{if } \max(\boldsymbol{m}) \geq \boldsymbol{V}_{\max} \end{cases} \tag{11}$$

$$s = \begin{cases} s, \text{if } s - s' < \Delta t \boldsymbol{A}_{\max} \\ s' + \Delta t \boldsymbol{A}_{\max}, \text{if } s - s' \geq \Delta t \boldsymbol{A}_{\max} \end{cases} \tag{12}$$

where s is the input for slave robot, s' is the input for slave robot in the previous step, $\boldsymbol{V}_{\max}$ and $\boldsymbol{A}_{\max}$ are the maximum translation and rotation speed and acceleration constraints for the needle mounted on the robot when the RCM is set on the needle tip, and Δt is the overhead for one control loop.

The intended difference in needle pose can be calculated as $\Delta t \boldsymbol{m}$. It should be taken into account that different instruments with different loads influence the motor dynamic character. Moreover, the different RCM point location on the needle with the same rotational speed will lead to different speeds for the piezo motor. In order to ensure that each of the motor joints are running on the safety critical mode within the fault tolerance, the position of joints obtained from the optical encoder sensors are used to check the deviation of the RCM. This deviation is calculated as

$$d_{rcm} = |\boldsymbol{x}_{rcm} - \boldsymbol{p}_{rcm}| \tag{13}$$

where p_{rcm} is the RCM position calculated from the joint position with forward kinematics. The $\boldsymbol{V}_{\max}$ will be reset online if the deviation exceeds the potential tolerance

$$\boldsymbol{V}_{\max} = \begin{cases} \boldsymbol{V}_{\max}, \text{if } d_{rcm} < \kappa\varepsilon \\ \max(\boldsymbol{m}), \text{if } d_{rcm} \geq \kappa\varepsilon \end{cases} \tag{14}$$

where $\kappa \in [0,1]$ is the security coefficient, and ε is the tolerance defined by clinic requirements.

D. Needle Insertion Depth Prediction

With the RCM control constraint, the needle will be relocated and will approach the subretinal target area. After the needle tip has approached the retinal surface, the control mode will be switched manually to needle insertion mode when only one DoF is moving. The needle insertion depth prediction is triggered when the injection movement starts. The OCT helps to capture a volume to track the needle insertion depth. The algorithm from Zhou *et al.* [27] is used to predict the needle tip depth under the retina with an accuracy of 16.5 μm. As shown in Fig. 6(a), the needle for subretinal injection has multiple segments with various geometrical features. While the OCT scanner is set to obtain the volumetric images (including the target area and the needle), the needle (32 G × 3 mm subretinal cannula from Eagle Labs Inc.) is segmented and reconstructed to eliminate the errors arising from the manufacture and transportation [27]. In order to archive robust calibration results, several OCT volumes are captured and averaged with estimated

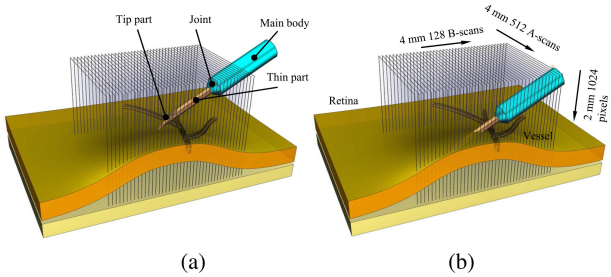

Fig. 6. OCT scan setup during needle insertion. (a) Needle is reconstructed when the needle is above the retina. (b) Needle tip is predicted during the insertion. The needle used has four main parts: tip part, thin part, joint, and main body.

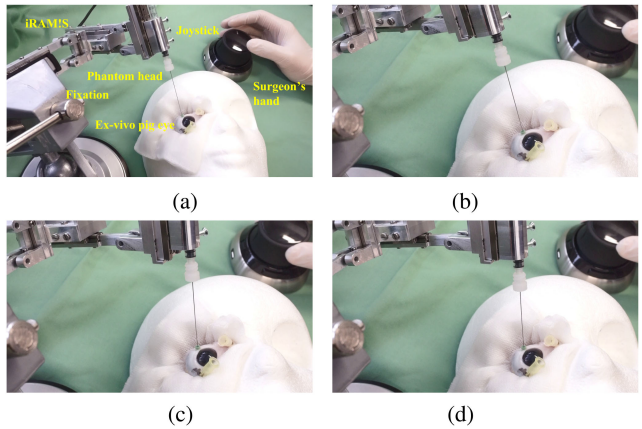

Fig. 7. Subretinal injection trail on the *ex-vivo* pig eye for busy mode control loop test. (a) Overall setup. The RCM control point will be registered with a button triggered on the joystick when the needle is inserted into the trocar. The trocar is placed on the sclera on the *ex-vivo* pig eye. (b) Needle is inserted into the *ex-vivo* eye. (c) Needle is pivoted around the insertion point to relocate the target area. (d) Final joint is only activated for high accuracy injection.

confidence interval evaluation with reference to the dimension of the needle. During the insertion, as shown in Fig. 6(b), the needle-tip position will be predicted based on the needle segment information above the retina. The distance between the retinal surface and the needle tip will also be calculated.

IV. Experiments and Results

We performed two sets of experiments with the proposed system. The first experiment is designed to verify the accuracy and safety performance of RCM, which is critical for any minimally invasive teleoperation system. The second experiment is the needle tracking during insertion when the needle is reconstructed and the needle tip is predicted under the retina to give the reference of the needle depth during the insertion. The *ex-vivo* pig eyes are obtained from the slaughter house directly before around three hours of experiments starting. All the eyes are preserved in the fresh water at the indoor temperature.

A. RCM Control Performance Evaluation

The performance of the RCM control is one of the most critical features to be evaluated for the system. The accuracy of the RCM control is directly related to the movement of each control loop. The control loop is decided by two factors, one is the control loop time and the other is the motor speed. The control loop time is critical since it influences the position accuracy of the robot and also adds the extra delay of human hand-eye reaction loop. The low interface of PID speed and position servo control runs on the firmware of the FPGA board with 10 KHz frequency. The joystick is connected to a host computer with a 2.8 GHz i7-7700HQ processor and 16 GB memory. To ensure the proposed system's real-time property, we implemented the control framework in C++ in Ubuntu 16.04 with real-time patches. The host computer communicates with FPGA low control board via an Ethernet connection to update the joint position and send the speed and position command. In order to test the control loop time of the designed system, we performed the experiments in a time period of 750 s with 50 000 control loops under two conditions: 1) idle mode, for which there is no input signal from the joystick; and 2) busy mode with continuous input signal from the joystick. The busy mode simulates the subretinal injection on the *ex-vivo* pig eye shown in Fig. 7. Fig. 8 shows that the idle

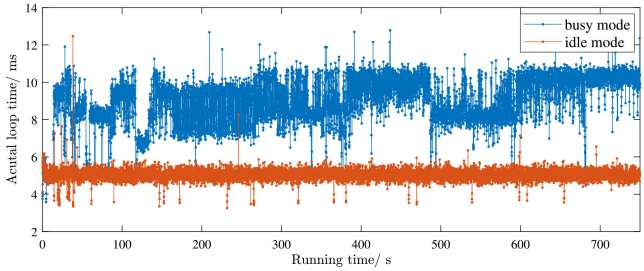

Fig. 8. Actual loop time with two modes test under 750 s.

mode control loop time is less than busy loop time because, in idle mode, no signal is updated and the motor control function is not called upon. The time for both of the two control loop modes is less than 14 ms which means we can fix the control loop time as 15 ms. This is significantly less than the surgeon's hand-eye reaction time which is around 200 ms [33].

Since each part of the robot is manufactured by a precision computer numerical control machine, the manufacturing accuracy of the parts can be considered to be within 5 μm. Therefore, we could infer the accuracy of RCM by calculating the forward kinematics with the joint positions of the robot. The optical encoder integrated into our piezo motors has a resolution of 0.05 μm. The algorithm control tolerance ε_1 and ε_2 are set to 1 μm to ensure accuracy from an algorithm calculation perspective. We tested various RCM positions along the needle with different λ to see the correlation of the motor speed and the RCM control deviation. The maximum rotation speed for the needle in RCM control is set to 12° per second. The RCM control error was 3 mm (maximum) with the suggestion from the medical doctor in the previous reference [6], [26]. However, due to the fact that the needle and trocar diameter are continuously decreasing for minimally invasive surgery, we set the error tolerance ε in (14) to 1 mm and the safety coefficient κ to 0.8. In order

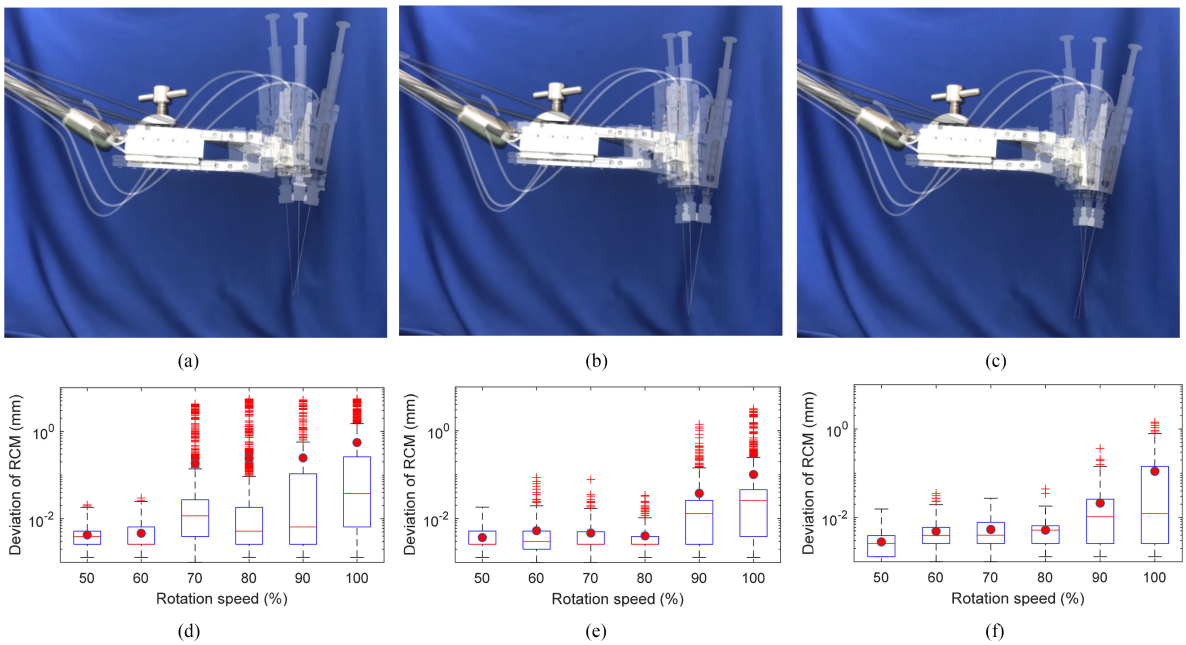

Fig. 9. Time-lapse photography for RCM control with different (a) $\lambda = 1.0$, (b) $\lambda = 0.8$, and (c) $\lambda = 0.6$ for the proposed method, while (d), (e), and (f) are the deviation d_rcm for (a), (b), and (c) with the maximum rotation speed, respectively. The whiskers show the minimum and maximum recorded change of the distance while the first and third quartile show the start and the end of the box. Band, red dot, and cross represent median, mean, and outliers of the recorded changes, respectively.

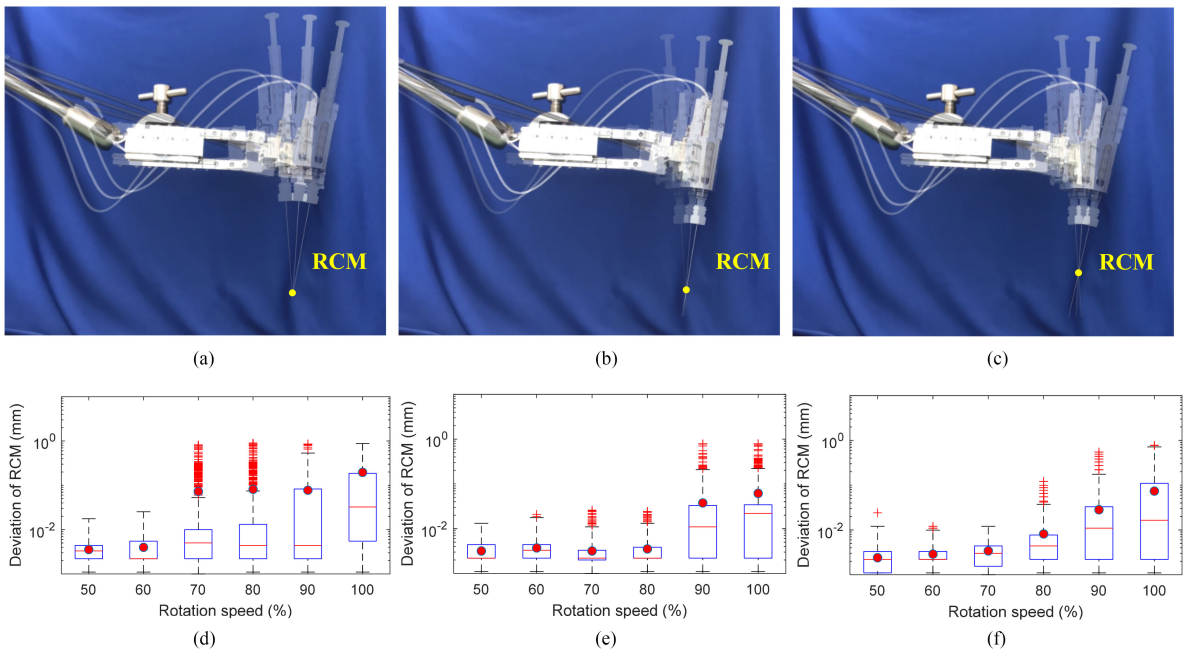

Fig. 10. Time-lapse photography for RCM control with different (a) $\lambda = 1.0$, (b) $\lambda = 0.8$, and (c) $\lambda = 0.6$ for the proposed method, while (d), (e), and (f) are the deviation d_rcm for (a), (b), and (c) with the maximum rotation speed, respectively. The yellow points in (a), (b), and (c) are the RCM control points. The whiskers show the minimum and maximum recorded change of the distance while the first and third quartile show the start and the end of the box. Band, red dot, and cross represent median, mean, and outliers of the recorded changes, respectively.

to show the effectiveness of the proposed method, two groups of experiment are preformed. One is the proposed method and the other one is the reference method without step size decrease and max speed update. The needle is pivoted around the RCM by 30°.

The time-lapse photography with different λ and whisker plots for RCM deviation using two different methods are shown in Figs. 9 and 10, respectively. As shown in the figures, A higher rotation speed under the same λ will lead to a greater RCM deviation, since we fixed the control loop time to a

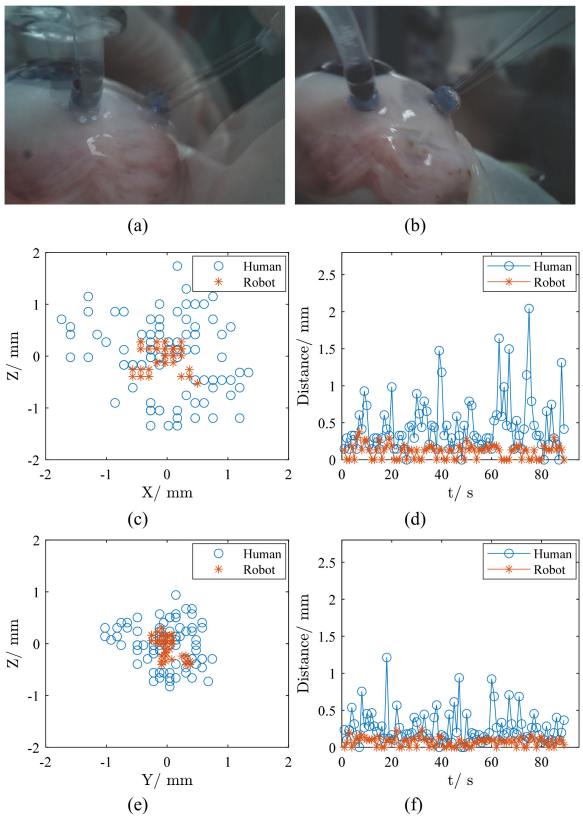

Fig. 11. RCM control performance of Human vs Robot. Time-lapse photography of the human (a) and robot (b) operation. (c) and (e) are the RCM points in two orthogonal camera in 90 s. (d) and (f) are the movement of RCM point with the interval of 1 s in 90 s.

certain value. Even though the pivoted speed is the same, the variance of λ will contribute to the different speed on the prismatic joint. This shows that with the same rotational speed, with a larger λ we observe larger deviation in average. Fig. 9 shows that the maximum RCM deviation can reach 5.5 mm for the reference method. However, Fig. 9 shows that the worst case of RCM deviation for the proposed method is restricted within 1.0 mm to ensure the safety and accuracy of RCM control. We can also observe tradeoff between the robot moving speed and RCM control accuracy, which the less RCM control could be also achieved with a slower moving speed of robot.

In order to verify the RCM performance further, we perform the test on the *ex-vivo* pig eye with the orthogonal camera setup. Two microscope cameras are placed in the orthogonal position related to the trocar. The RCM point is defined as the entry point of the trocar. To demonstrate the superiority of the robot RCM control, an experienced surgeon was asked to perform the same motion manually which tracks a vessel on the retinal. Fig. 11 demonstrates the RCM point tracking results of the human versus robot. The time-lapse photography for the human is more blur than the robot due to inaccuracy RCM control and tremor from surgeon's hand. The largest RCM control deviation is 2.11 and 0.39 mm for the human and robot operation, respectively. During the test, the robot has the rotation speed lower than 6° per second which means that the RCM deviation in theoretical is less than 0.1 mm as shown in Fig. 10. This contradiction

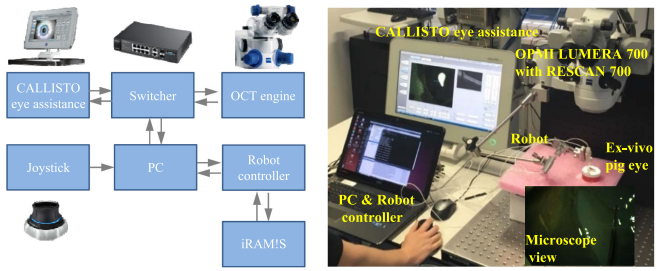

Fig. 12. Experimental setup for injection depth tracking.

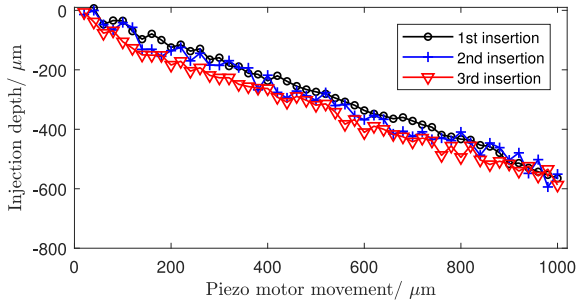

Fig. 13. Needle insertion tracking using the robot on the tissue phantom three times.

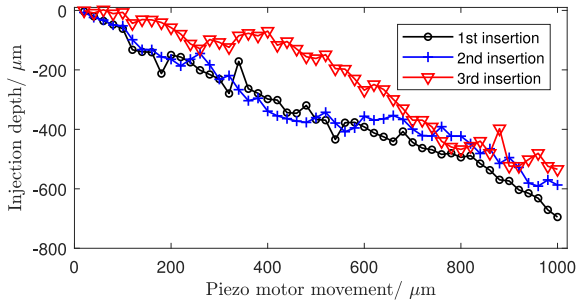

Fig. 14. Needle insertion tracking using the robot on the *ex-vivo* pig eye three times.

could mainly come from the interaction of trocar and needle during the movement. Due to the fact that the trocar is a cylinder, the contact of needle and trocar is not a single point which will cause drag force and distortion of tissue and needle during needle pivoting around RCM point.

B. Experiment of Injection Depth Tracking

After verifying the accuracy and safety performance of RCM control, we performed experiments for needle insertion depth tracking with OCT volumetric images. The experimental setup is shown in Fig. 12. The robot is mounted on an adjustment bracket and the motion of the robot is controlled by a robot controller with input from the joystick. The OPMI LUMERA 700 with integrated RESCAN 700 intraoperative OCT engine is fixed on the optical table to reduce the influence of the ambient vibration. The adjustment bracket is also rigidly connected to the optical table to minimize the relative movement of the robot

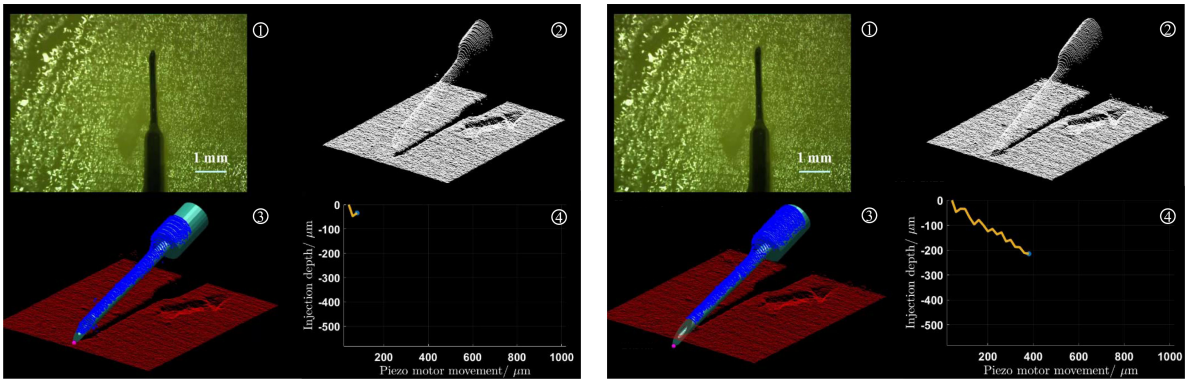

Fig. 15. Needle insertion using the robot on the tissue phantom: (a) motor advances 60 μm; (b) motor advances 380 μm. ① is the microscope view. ② is the original OCT cube with rendering the surface point cloud. ③ is the predicted needle pose and position by using method from [27]. The needle CAD model is fitted to the needle point cloud in blue color. The phantom tissue surface is segmented as red color. The needle tip point is marked as the purple point. ④ is the needle insertion depth tracking between the motor movements and needle tip insertion prediction.

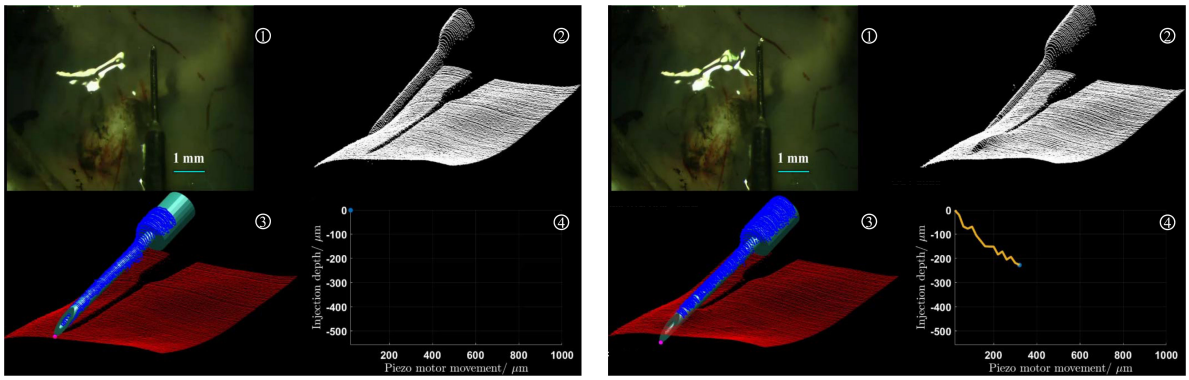

Fig. 16. Needle insertion using the robot on the ex-vivo pig eye: (a) motor advances 20 μm; (b) motor advances 360 μm. ① is the microscope view. ② is the original OCT cube with rendering the surface point cloud of retina on the ex-vivo pig eye. ③ is the predicted needle pose and position by using method from [27]. The needle CAD model is fitted to the needle point cloud in blue color. The retina surface is segmented as red color. The needle tip point is marked as the purple point. ④ is the needle insertion depth tracking between the motor movements and needle tip insertion prediction.

base and the OCT engine. A foot panel is used to relocate the OCT scan area. The OCT is set to operate with the maximum available scanning speed (27 000 A-scans per second), in a cube resolution of $128 \times 512 \times 1024$ pixels. The implementation of our approach is executed on the *CALLISTO* eye assistance computer system with an Intel Core i7 CPU and an NVIDIA GeForce GTX 980i GPU with an average speed of 0.4 s for each cube with parallel programming.

In the first phase of the experiments, the robot is adjusted manually by the adjustment bracket and is then controlled by the joystick for approaching the needle tip to the retina. During the injection, only the motor that is holding the syringe is enabled for needle positioning. In the beginning, we captured five OCT cubes for needle reconstruction and calibration [27]. Each scan takes 1.5 and 0.3 s for processing a single cube. Thereafter, the motor is programmed to move exactly 20 μm in each step and the OCT cube is captured after each movement. Each step takes 2.5 s including motor movement, cube scan, and process. When the predicted needle tip distance to the surface is less than 20 μm we assume that the needle starts puncturing the tissue, then the motor advances an additional 50 steps. Each step takes 3.0 s including motor movement, cube scan, and process. The whole insertion process will cost around 5 minutes. We repeated the same workflow for the tissue phantom (40% fat cheese) and *ex-vivo* pig eyes three times each. Figs. 13 and 14 show the tracking for the needle tip to the retinal surface distance on phantom tissue and *ex-vivo* pig eye three times, respectively. Both images show that there is an approximately linear increase between motor movement and insertion depth. However, the tissue phantom has a better linear performance than the pig eyes. During the needle insertion, the interaction between the needle and tissue is very complicated, causing stochastic deformation of the tissue. This deformation has a larger impact on the retina in the pig eye, since retina tissue (with an elastic constant around 2.0 mm/N [34]) is greater elastic than the phantom tissue (with an elastic constant around 0.67 mm/N [35]) which is made of soft cheese. Therefore, the fluctuation of the insertion depth during tracking is more on the biotissue, in addition to the influence of the result of distance measurement errors.

Figs. 15 and 16 show sequences of the insertion progress. The reconstruction results appropriately match with the needle tip status in the en-face image from the microscope.

In the microscopic image, it is almost impossible to estimate the needle tip position. However, with the proposed system, we show that using the robot as the assistant as well as with the OCT volumetric imaging, the needle tip can be visualized and injection depth calculated precisely. The degree of deformation can also be visualized. Since the robot is holding the needle with RCM control, the surgeon is free from the dexterous motion and hand tremor. The precision of the robot can also help surgeons break through their physical limitations for performing impossible tasks, and open up new interventional possibilities. The visualization has the potential to assist surgeons in making more efficient decisions during the subretinal injection, and may also make it possible to investigate how much insertion is appropriate for the best outcome.

V. Conclusion

This article presented our novel system for assisting ophthalmologists in performing the difficult task of subretinal injection using soft RCM with 5 DoF robot with the hybrid parallel–serial mechanism. In this article, intraoperative OCT volumetric imaging was used to enhance the visual feedback. The safety and accuracy of RCM was evaluated on the robot with tissue phantom and *ex-vivo* pig trials. The evaluation results showed that the single control loop of the system is executed in 15 ms and the RCM control accuracy could be ensured within 1 mm, both of which were within the clinical range. Finally, we tested the robotic subretinal insertion on the *ex-vivo* pig eye and phantom tissue to verify the visualization benefits for the surgeon. With the help of the robot, surgeons could put more effort to be the decision makers during the operation rather than spending too much time on improving their surgical skills to cope with hand tremors and dexterous motion. Our future work will focus on an injection path planning and trajectory design in a way that allows the drug to be delivered directly and precisely to subretinal target areas defined preoperatively, avoiding critical obstacles like retinal vessels and the RPE layer. Further work will also consider the challenges from the *in-vivo* retinal surgery.

References

[1] S. Parikh, A. Le, J. Davenport, M. B. Gorin, S. Nusinowitz, and A. Matynia, "An alternative and validated injection method for accessing the subretinal space *via* a transcleral posterior approach," *J. Vis. Exp.*, no. 118, 2016, Art. no. e54 808.

[2] K. Xue *et al.*, "Beneficial effects on vision in patients undergoing retinal gene therapy for choroideremia," *Nature Med.*, vol. 24, no. 10, pp. 1507–1512, 2018.

[3] R. Casten, B. W. Rovner, and J. L. Fontenot, "Targeted vision function goals and use of vision resources in ophthalmology patients with age-related macular degeneration and comorbid depressive symptoms," *J. Vis. Impaired Blindness*, vol. 110, no. 6, pp. 413–424, 2016.

[4] W. L. Wong *et al.*, "Global prevalence of age-related macular degeneration and disease burden projection for 2020 and 2040: a systematic review and meta-analysis," *Lancet Global Health*, vol. 2, no. 2, pp. e106–e116, 2014.

[5] K. Xue, M. Groppe, A. Salvetti, and R. MacLaren, "Technique of retinal gene therapy: delivery of viral vector into the subretinal space," *Eye*, vol. 31, no. 9, pp. 1308–1316, 2017.

[6] T. Nakano, N. Sugita, T. Ueta, Y. Tamaki, and M. Mitsuishi, "A parallel robot to assist vitreoretinal surgery," *Int. J. Comput. Assist. Radiol. Surg.*, vol. 4, no. 6, pp. 517–526, 2009.

[7] W. T. Ang, C. N. Riviere, and P. K. Khosla, "Design and implementation of active error canceling in hand-held microsurgical instrument," in *Proc. Intell. Robot. Syst. IEEE/RSJ Int. Conf.*, 2001, vol. 2, pp. 1106–1111.

[8] W. Wei, R. Goldman, N. Simaan, H. Fine, and S. Chang, "Design and theoretical evaluation of micro-surgical manipulators for orbital manipulation and intraocular dexterity," in *Proc. Robot. Autom. IEEE Int. Conf.*, 2007, pp. 3389–3395.

[9] R. Taylor *et al.*, "A steady-hand robotic system for microsurgical augmentation," *Int. J. Rob. Res.*, vol. 18, no. 12, pp. 1201–1210, 1999.

[10] F. Ullrich *et al.*, "Mobility experiments with microrobots for minimally invasive intraocular Surgery Microrobot experiments for intraocular surgery," *Investigative Ophthalmol. Vis. Sci.*, vol. 54, no. 4, pp. 2853–2863, 2013.

[11] H. C. M. Meenink, R. Rosielle, M. Steinbuch, H. Nijmeijer, and M. C. De Smet, "A master-μ slave robot for vitreo-retinal eye surgery," in *Proc. Euspen Int. Conf.*, 2010, pp. 3–6.

[12] E. Rahimy, J. Wilson, T. C. Tsao, S. Schwartz, and J. P. Hubschman, "Robot-assisted intraocular surgery: development of the IRISS and feasibility studies in an animal model," *Eye*, vol. 27, no. 8, pp. 972–978, 2013.

[13] A. Gijbels, E. Vander Poorten, B. Gorissen, A. Devreker, P. Stalmans, and D. Reynaerts, "Experimental validation of a robotic comanipulation and telemanipulation system for retinal surgery," in *Proc. 5th IEEE RAS EMBS Int. Conf. Biomed. Robot. Biomechatronics*, 2014, pp. 144–150.

[14] C. N. Riviere, W. T. Ang, and P. K. Khosla, "Toward active tremor canceling in handheld microsurgical instruments," *IEEE Trans. Robot. Autom.*, vol. 19, no. 5, pp. 793–800, Oct. 2003.

[15] C. Song, P. L. Gehlbach, and J. U. Kang, "Active tremor cancellation by a smart handheld vitreoretinal microsurgical tool using swept source optical coherence tomography," *Opt. Express*, vol. 20, no. 21, pp. 23 414–23 421, 2012.

[16] A. Molaei *et al.*, "Toward the art of robotic-assisted vitreoretinal surgery," *J. Ophthalmic Vis. Res.*, vol. 12, no. 2, pp. 212–218, 2017.

[17] T. Edwards *et al.*, "First-in-human study of the safety and viability of intraocular robotic surgery," *Nature Biomed. Eng.*, vol. 2, pp. 649–656, 2018.

[18] R. Muradore and P. Fiorini, "A PLS-based statistical approach for fault detection and isolation of robotic manipulators," *IEEE Trans. Ind. Electron.*, vol. 59, no. 8, pp. 3167–3175, Aug. 2012.

[19] H. Arai, K. Tanie, and S. Tachi, "Path tracking control of a manipulator considering torque saturation," *IEEE Trans. Ind. Electron.*, vol. 41, no. 1, pp. 25–31, Feb. 1994.

[20] N. Rieke *et al.*, "Real-time localization of articulated surgical instruments in retinal microsurgery," *Med. Image Anal.*, vol. 34, pp. 82–100, 2016.

[21] M. A. Nasseri *et al.*, "The introduction of a new robot for assistance in ophthalmic surgery," in *Proc. IEEE 35th Annu. Int. Conf. Eng. Med. Biol. Soc.*, 2013, pp. 5682–5685.

[22] R. H. Taylor, J. Funda, D. D. Grossman, J. P. Karidis, and D. A. LaRose, "Remote center-of-motion robot for surgery," U.S. Patent 5 397 323A, Mar. 14, 1995.

[23] D. Kim, E. Kobayashi, T. Dohi, and I. Sakuma, "A new, compact MR-compatible surgical manipulator for minimally invasive liver surgery," in *Proc. Int. Conf. Med. Image Comput. Comput.-Assisted Intervention*, 2002, pp. 99–106.

[24] W. Wei, R. E. Goldman, H. F. Fine, S. Chang, and N. Simaan, "Performance evaluation for multi-arm manipulation of hollow suspended organs," *IEEE Trans. Robot.*, vol. 25, no. 1, pp. 147–157, Feb. 2009.

[25] H. Yu, J.-H. Shen, K. M. Joos, and N. Simaan, "Design, calibration and preliminary testing of a robotic telemanipulator for OCT guided retinal surgery," in *Proc. Robot. Autom. IEEE Int. Conf.*, 2013, pp. 225–231.

[26] T. Sakai *et al.*, "Design and development of miniature parallel robot for eye surgery," in *Proc. IEEE 36th Annu. Int. Conf. Eng. Med. Biol. Soc.*, 2014, pp. 371–374.

[27] M. Zhou *et al.*, "Precision needle tip localization using optical coherence tomography images for subretinal injection," in *Proc. IEEE Int. Conf. Robot. Autom.*, 2018, pp. 1–8.

[28] X. He, M. Balicki, P. Gehlbach, J. Handa, R. Taylor, and I. Iordachita, "A multi-function force sensing instrument for variable admittance robot control in retinal microsurgery," in *Proc. IEEE Int. Conf. Robot. Autom. (ICRA)*, 2014, pp. 1411–1418.

[29] M. Waine, C. Rossa, R. Sloboda, N. Usmani, and M. Tavakoli, "3D shape visualization of curved needles in tissue from 2D ultrasound images using RANSAC," in *Proc. IEEE Int. Conf. Robot. Autom (ICRA)*, 2015, pp. 4723–4728.

[30] Y.-J. Jo, D.-W. Heo, Y.-I. Shin, and J.-Y. Kim, "Diurnal variation of retina thickness measured with time domain and spectral domain optical coherence tomography in healthy subjects," *Investigative Ophthalmol. Vis. Sci.*, vol. 52, no. 9, pp. 6497–6500, 2011.
[31] M. Zhou *et al.*, "Towards robotic eye surgery: Marker-free, online hand-eye calibration using optical coherence tomography images," *IEEE Robot. Autom. Lett.*, vol. 3, no. 4, pp. 3944–3951, Oct. 2018.
[32] G.-W. Cheon, Y. Huang, and J. U. Kang, "Active depth-locking handheld micro-injector based on common-path swept source optical coherence tomography," *Proc. SPIE.* vol. 9317, 2015, Art. no. 93 170U.
[33] M. Pfister *et al.*, "Comparison of reaction response time between hand and foot controlled devices in simulated microsurgical testing," *BioMed Res. Int.*, vol. 2014, 2014, Art. no. 769296.
[34] I. Jones, M. Warner, and J. Stevens, "Mathematical modelling of the elastic properties of retina: A determination of Young's modulus," *Eye*, vol. 6, no. 6, pp. 556–559, 1992.
[35] M. Charalambides, J. Williams, and S. Chakrabarti, "A study of the influence of ageing on the mechanical properties of cheddar cheese," *J. Mater. Sci.*, vol. 30, no. 16, pp. 3959–3967, 1995.

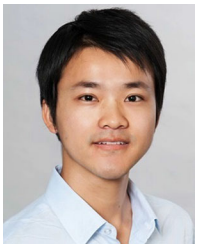

Mingchuan Zhou received the B.Eng. degree in agricultural mechanization engineering from Northeast Agriculture University, Harbin, China, in 2012 and the M.Eng. degree from Zhejiang University, Hangzhou, China, in 2015. He is currently working toward the Ph.D. degree in computer science with the Chair of Robotics, Artificial Intelligence and Real-time Systems at the Department of Computer Science of the Techical University of Munich, Munich, Germany.

His research interests include the autonomous system, medical robotics, image processing, and agricultural robotics.

Mr. Zhou was the recipient of Finalist of Best Paper Awards IEEE-ROBIO in 2017.

Qiming Yu received the B.S. degree in mechanical engineering from Zhejiang University, Zhejiang, China, in 2016, and the M.S. degree in mechanical engineering from the Technical University of Munich, Germany, in 2019.

His research interests include control theory and collaborative robotics.

Kai Huang recieved the B.Sc. degree from Fudan University, Shanghai, China, in 1999, the M.Sc. degree from the University of Leiden, Leiden, The Netherlands, in 2005, and the Ph.D. degree from ETH Zurich, Switzerland, in 2010, all in computer science.

He joined Sun Yat-Sen University, Guangzhou, China, as a Professor in 2015. He was appointed as the Director of the Institute of Unmanned Systems of School of Data and Computer Science in 2016. His research interests include techniques for the analysis, design, and optimization of embedded systems, particularly in the automotive domain.

Dr. Huang was the recipient of Best Paper Awards ESTIMedia in 2013, International Conference on Embedded Computer Systems: Architectures, Modeling, and Simulation (SAMOS) 2009, and General Chairs Recognition Award for Interactive Papers in IEEE Conference on Decision and Control (CDC) in 2009.

Simeon Mahov received the B.S. degree in mechanical engineering from the Georgia Institute of Technology, Atlanta, GA, USA, in 2014. He is currently working toward the master's degree in computational science and engineering with the Technical University of Munich, Munich, Germany.

His research interests include machine learning and robot control.

Abouzar Eslami received the Ph.D. degree in electrical engineering from the Sharif University of Technology, Tehran, Iran, in 2010.

From 2011 to 2013, he was a Postdoctoral Researcher with the Chair for computer Aided Medical Procedures and Augmented Reality Technical University of Munich, Munich, Germany. Afterwards, he was a Project Manager of interventional imaging in Carl Zeiss Meditec AG, Jena, Germany. He is currently the Head of Translational Research Lab at Carl Zeiss Meditec AG.

His research interests include registration/visualization, segmentation, reconstruction, medical imaging, and machine learning for medical applications.

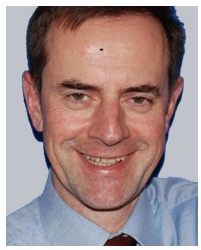

Mathias Maier received the Ph.D. degree in medicine at the Klinikum rechts der Isar of Technical University of Munich (TUM).

He is a Senior Physician and Deputy Director at the Eye Clinic at the Klinikum rechts der Isar of the TUM. His specialties include dermal and vitreous surgery, cataract surgery, diagnostics, and treatment of macular disease. He has taken part in numerous multicenter studies to treat macular degeneration and macular edema.

Chris P. Lohmann received the Ph.D. degrees in Gießen, Germany, in 1991, and in London, U.K., in 1995, and the postdoctoral teaching qualification (habilitation) degree in Regensburg, Germany, in 2000.

From 2004 to 2005, he was an Acting Head of the Department of Ophthalmology, Klinikum rechts der Isar, Technical University Munich (TUM) University Hospital. Since 2002, he has been an Adjunct Professor with the Eye Research Institute, University of Ottawa, Ottawa, ON, Canada. Since 2005, he has been the Director of the Department of Ophthalmology, TUM, where he held a W3 Professorship position. His research interests include corneal diseases and refractive surgery.

Nassir Navab received the doctoral degree in computer and automation from INRIA / Paris XI, Paris, France.

He did two years of Postdoctoral research with the MIT Media Laboratory in Cambridge, MA, USA. Prior to becoming a Full Professor with the Technical University of Munich, Munich, Germany in 2003, he was a distinguished member of the technical staff at Siemens Corporate Research (SCR) in Princeton, NJ, USA. His research interests include computer-aided medical procedures and augmented reality. The work involves developing technologies to improve the quality of medical intervention and bridges the gap between medicine and computer science.

Dr. Navab became a Board Member of Medical Image Computing and Computer Assisted Intervention (MICCAI) in 2006. He is on the Editorial Board of many international journals, including IEEE TRANSACTIONS ON MEDICAL IMAGING, *MedIA*, and *Medical Physics*.

Daniel Zapp received the doctorate degree in human medicine from the Department of Ophthalmology Mathildenstrasse, Ludwig-Maximilians-University Munich, Munich, Germany.

He is now a Senior Consultant with the Department of Ophthalmology with the Technical University of Munich, Munich, since 2008, and also is working abroad with Mount Sinai Hospital, New York, NY, USA. His research interests include cornea and glaucoma.

Dr. Zapp was the recipient of the First Prize in the European Specialist Certificate (FEBO). He was also awarded the prize in October 2014 by the German Ophthalmological Society as the Best German Participant.

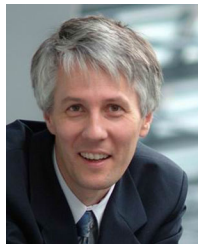

Alois Knoll received the M.Sc. degree in electrical /communications engineering from the University of Stuttgart, Stuttgart, Germany, in 1985, and the Ph.D. (summa cum laude) degree in computer science from the Technical University of Berlin (TU), Berlin, Germany, in 1988.

He served on the faculty of the Computer Science Department of TU Berlin until 1993, when he qualified for teaching computer science at a university (habilitation). Following this, he was a Full Professor and the Director of the Computer Engineering research group at the University of Bielefeld until 1991, when he assumed the Professorship of Real-Time Systems and Robotics at Technical University of Munich, Munich, Germany. His research interests include cognitive, medical and sensor-based robotics, multiagent systems, data fusion, adaptive systems, multimedia information retrieval, model-driven development of embedded systems with applications to automotive software and electric transportation, and simulation systems for robotics and traffic.

M. Ali Nasseri received the Ph.D. degree in biomedical engineering with a joint degree from the Medical School, Mechanical Engineering Faculty and Informatics Faculty of the Technical University of Munich, Munich, Germany, in 2015.

He is currently the Head of the Medical Technology Laboratory at the Ophthalmology Department of Klinikum rechts der Isar which is the university hospital of the Technical University of Munich. He has authored or coauthored more than 50 scientific publications, patents, and book chapters. His research interests include surgical robotics, medical imaging, machine learning and translation of these technologies to the healthcare system.

Dr. Nasseri is an active member of Association for Research in Vision and Ophthalmology and deutsche ophthalmologische gesellschaft (DOG).